ADVANCED MATERIALS
www.advmat.de

Advanced Optical Programming of Individual Meta-Atoms Beyond the Effective Medium Approach

Ann-Katrin U. Michel, Andreas Heßler, Sebastian Meyer, Julian Pries, Yuan Yu, Thomas Kalix, Martin Lewin, Julian Hanss, Angela De Rose, Tobias W. W. Maß, Matthias Wuttig, Dmitry N. Chigrin, and Thomas Taubner**

Nanometer-thick active metasurfaces (MSs) based on phase-change materials (PCMs) enable compact photonic components, offering adjustable functionalities for the manipulation of light, such as polarization filtering, lensing, and beam steering. Commonly, they feature multiple operation states by switching the whole PCM fully between two states of drastically different optical properties. Intermediate states of the PCM are also exploited to obtain gradual resonance shifts, which are usually uniform over the whole MS and described by effective medium response. For programmable MSs, however, the ability to selectively address and switch the PCM in individual meta-atoms is required. Here, simultaneous control of size, position, and crystallization depth of the switched phase-change material (PCM) volume within each meta-atom in a proof-of-principle MS consisting of a PCM-covered Al–nanorod antenna array is demonstrated. By modifying optical properties locally, amplitude and light phase can be programmed at the meta-atom scale. As this goes beyond previous effective medium concepts, it will enable small adaptive corrections to external aberrations and fabrication errors or multiple complex functionalities programmable on the same MS.

Metasurfaces (MSs) consist of periodically arranged metallic or dielectric elements ("meta-atoms") of subwavelength size. The individual properties of each resonant meta-atom collectively facilitate the control of the impinging light.[1] For active MSs with freely adjustable optical properties, materials which can be actively manipulated by external stimuli, such as stress,[2] heat,[3] electrostatic,[4,5] or magnetic forces[6] must be used. Graphene,[7] gallium arsenide (GaAs),[8] indium antimony (InSb),[9] and vanadium dioxide (VO_2)[10,11] have been successfully employed for volatile resonance tuning. However, these materials cannot easily be used to change the optical properties of each meta-atom individually in the visible and infrared spectral range because it would require a constant application of voltage or heat on sub-wavelength scales leading to excessive use of conductive connections, which could interfere with the optical response of the MSs. Tuning MSs on a meta-atom or sub-meta-atom scale becomes possible when utilizing phase-change materials (PCMs). These materials are commonly used for nonvolatile optical and electrical data storage because of the huge property contrast between their amorphous (A) and crystalline (C) phases[12] resulting from a unique bonding mechanism.[13,14] This makes them ideally suited for photonic applications ranging from integrated optical memories over color displays to active MSs.[15] For example, they have already been designed and successfully employed for applications such as polarization filtering,[16] lensing,[17] and beam steering.[18–20]

Commonly, active infrared MSs based on PCMs exhibit different operation states by switching the entire MS via heating[19,21–24] and short electrical[25] or optical pulses.[17,26] Intermediate states of the PCM crystallization have also been exploited to obtain partial resonance shifts[27,28] by adjusting the annealing conditions. Microscopically, these states are determined by the random distribution of nanoscale crystallites in the PCM layer, while macroscopically they are typically treated within effective medium theory. In order to go beyond the effective medium approach, a well-defined spatial distribution of crystalline volumes is desirable. As known from rewritable CDs and DVDs, sub-micrometer-sized crystalline spots can be optically written into thin amorphous PCM films, and vice versa.[12,29,30] Irradiation with a laser causes heat to accumulate in the PCM layer due to optical absorption. The heat provides the energy to structurally transform the PCM into a crystalline phase. Depending on the local temperature and its

Dr. A.-K. U. Michel,[+] A. Heßler, S. Meyer, J. Pries, Dr. Y. Yu, T. Kalix, M. Lewin, J. Hanss, A. De Rose, Dr. T. W. W. Maß, Prof. M. Wuttig, Dr. D. N. Chigrin, Prof. T. Taubner
I. Institute of Physics (IA)
RWTH Aachen University
D-52056 Aachen, Germany
E-mail: hessler@physik.rwth-aachen.de; taubner@physik.rwth-aachen.de
Dr. D. N. Chigrin
DWI – Leibniz Institute for Interactive Materials
Forckenbeckstr. 50, D-52056 Aachen, Germany
The ORCID identification number(s) for the author(s) of this article can be found under https://doi.org/10.1002/adma.201901033.

[+]Present address: Optical Materials Engineering Laboratory, Department of Mechanical and Process Engineering, ETH Zurich, 8092 Zurich, Switzerland

DOI: 10.1002/adma.201901033

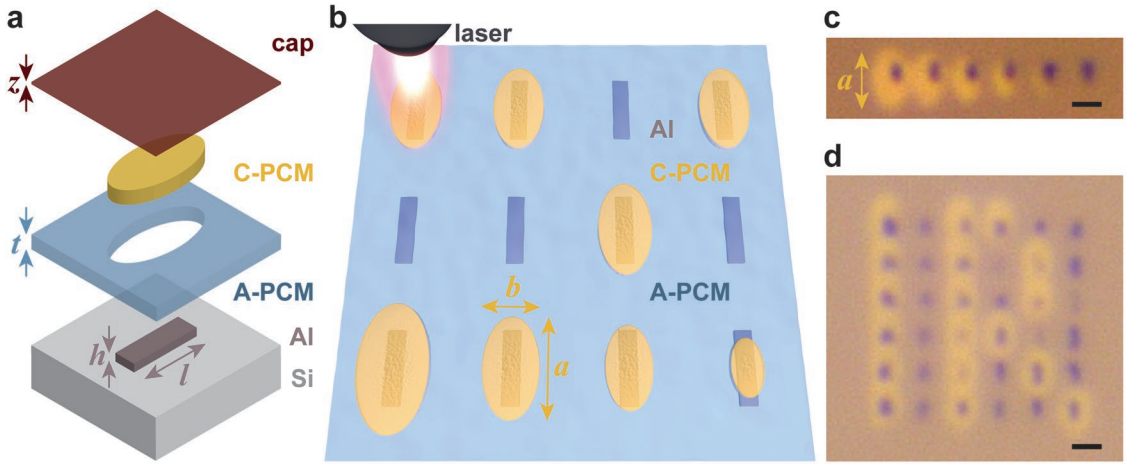

Figure 1. Local addressing concept. a) Sketch of the sample layer stack: Si substrate (gray), Al antenna (dark gray) with height h and length l, A-PCM layer (blue, thickness t) with the C-PCM spot (yellow) and protective capping layer (dark red, thickness z). b) Schematic view of an Al nanorod antenna array covered with A-PCM. Selected antennas are locally addressed with a laser with an elliptical beam profile, resulting in C-PCM spots of different sizes (axes a and b, yellow). c) Light microscope image of GST-326 covered Al nanorods locally addressed with C-spots of decreasing size. d) Light microscope image of locally addressed GST-326 covered nanorods. The C-spots have the same size and spell out "IR." The scale bars equal 1 µm.

history, this can lead to rapid crystallization, with the maximum crystallization velocities being reached between the glass transition temperature and the melting temperature of the material. Optical addressing has been recently utilized to fabricate dielectric MSs.[17,31] Here, we introduce a new concept for optical programming of individual meta-atoms in the IR spectral range. We show how to control the lateral size and crystallization depth of a fully switched PCM volume inside of each sub-wavelength meta-atom by adjusting the pulse parameters of a visible switching laser.

By using visible light for switching an infrared MS, we can modify the PCM phase on length scales smaller than the size of the fabricated meta-atom. Our meta-atoms consist of aluminum nanorods (width w = 157 nm, length l = 642 nm and height h = 30 nm) arranged in a square array (period p = 1259 nm) on a silicon substrate. The whole sample is covered by a thin film of amorphous $Ge_3Sb_2Te_6$[21,32] (A-GST-326, thickness t = 75 nm) and a protective capping layer of $(ZnS)_{80}$–$(SiO_2)_{20}$ with z = 10 nm (**Figure 1**a). Upon phase change, the real part of the GST-326 refractive index changes from $\underline{n}_A = 3.5$ to $\underline{n}_C = 6.1$ at 2000 cm^{-1}.[33] In Figure 1b, we illustrate the principle of local addressing and control of the crystalline spot (C-spot) size, which we achieved by applying single sub-microsecond laser pulses of different pulse power and constant pulse duration with a wavelength λ = 660 nm (cf. Experimental Section, Supporting Information). The local increase on the refractive index in the medium around the rod antennas causes a redshift of their resonance frequency toward lower frequencies. To better match the elongated rod shape of the antennas, we employ a laser diode, which generates an elliptical laser spot (cf. Experimental Section). Irradiation with this elliptical laser spot crystallizes the A-GST in an elliptical area (C-spot). While the shape of the C-spot remains elliptical (a/b = const.), its size is dependent on the laser parameters (cf. Supporting Information). As sketched in the bottom row of Figure 1b, we could successively decrease the C-spot size, which is experimentally demonstrated in Figure 1c. Local addressing is shown in Figure 1d, where C-spots are only written on selected nanoantennas, spelling the letters IR. Reversible switching is also possible (cf. Supporting Information).

Simulated relative reflection spectra of identically switched antenna arrays with different C-spot sizes all show clear resonant behavior (**Figure 2**a). Depending on the size of the C-spots (color coded for the long spot axis a), the resonance frequencies shift from ν_{res} = 2028 cm^{-1} (vertical blue line) in the amorphous case to 1692 cm^{-1} (vertical yellow line) in the fully crystalline case. The larger the C-spot, the lower the resonance frequency ν_{res}. However, this behavior is not linear, which is emphasized by the inset of Figure 2a. There, the resonance shift $\Delta\nu_{res}$ with respect to the amorphous state is shown for different C-spot sizes a. The resonance shift between two successive sizes a is largest for $a \approx l$, where l is the antenna length. This is related to the strong local fields at the antenna tips in resonance.[34] The measured relative reflectance spectra of differently switched 6 × 6 antenna arrays are shown in Figure 2b. The C-spot size has been controlled by adjusting the laser power employed to switch the material (Figure 2c, Experimental Section). The resonance frequency decreases with increasing spot size, from ν_{res} = 2006 cm^{-1} in the fully amorphous case down to ν_{res} = 1711 cm^{-1} for the largest spots. The resulting resonance shifts are given as a function of the C-spot size a in the inset of Figure 2b. In line with our expectations, the curve of the resonance shift has the largest slope for $a \approx l$. For the largest studied spot size a = 3.19 µm, we achieved a total shift $\Delta\nu_{res}$ = 295 cm^{-1}. Overall, this experimentally demonstrates that we can continuously tune the resonances of PCM-covered nanoantennas by controlling the size of the crystalline regions inside of one meta-atom.

While the experimental C-spot-size-dependent resonance shifting behavior qualitatively matches the predicted one, there is a quantitative discrepancy: Although the largest simulated C-spot sizes ($a > 3l$) show a saturation of the calculated resonance shift $\Delta\nu_{res}$ in the inset of Figure 2a, the measured shift reaches only about 60% of this value at $a \approx 3l$ and continues to increase for larger a. Only after fully crystallizing the sample by annealing it in an oven at 180 °C for 30 min, a comparable maximum resonance

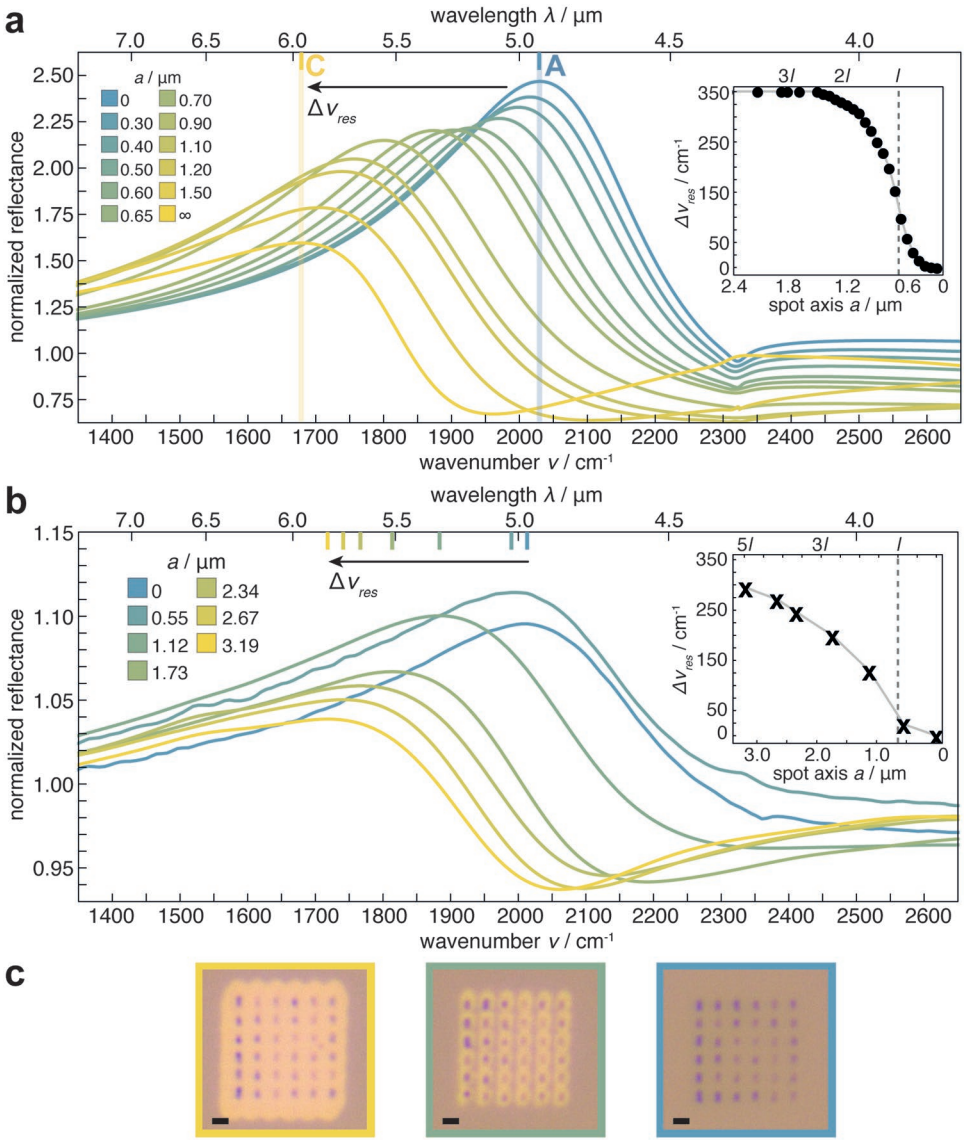

Figure 2. Resonance tuning by local addressing. a) Simulated normalized reflectance spectra of an infinite antenna array covered with A-GST-326 (geometry as in Figure 1a). Each antenna in the array is switched with centered C-spots of size a (color-coded). All curves show a clear resonance, which shifts from $\nu_{res} = 2028$ cm^{-1} (vertical blue line) in the amorphous case to 1692 cm^{-1} (vertical yellow line) in the fully crystalline case. The inset shows the resonance shift $\Delta\nu_{res}(a) = \nu_{res}(a) - \nu_{res}(0\ \mu m)$ with respect to the amorphous state. Its slope is largest for $a \approx l$ (dashed gray line) because of the strong local fields at the antenna tips in resonance. b) Normalized FTIR reflectance spectra of (6 × 6) antenna arrays covered and switched according to A. The resonance frequency positions are marked by colored ticks on the top, an arrow indicating the resonance shift $\Delta\nu_{res}$, while $\Delta\nu_{res}(a)$ is shown as inset. The largest increase in resonance shift is measured for $a \approx l$ (dashed gray line). c) Optical microscope images of the antenna arrays corresponding to three different spectra for a = 0, 1.73, 3.19 µm (colored frame according to legend in panel b). The scale bars equal 1 µm.

shift was achieved (exp.: 362 cm^{-1} vs sim.: 336 cm^{-1}, Supporting Information). This discrepancy between our initial simulations and the experiments could be a hint for the importance of the switching dynamics at smaller length scales.

In order to understand this apparent difference, we have to investigate the 3D nature of the optically induced crystallization and its consequences for the MS resonance tuning. The highly nonlinear relation between temperature and crystallization speed in PCMs combined with the short time scales of the optical switching leads to the process being dominated by spatially inhomogeneous and nonequilibrium temperature distributions. This results in crystallization depths that strongly depend on the temperature gradient in the PCM layer, which can only accurately be determined using self-consistent multiphysics simulations. In a first approximation for this complicated multiphysics problem, we performed simulations where we varied the crystallization depth of the C-spots by approximating them as elliptical cylinders with a height d (corresponding to the crystallization depth) smaller than the whole GST-film thickness t (**Figure 3**a). The resulting resonance shifts $\Delta\nu_{res}(d,a)$ for each crystallization depth d (color-coded) against the spot size a are shown in Figure 3b. An increasing

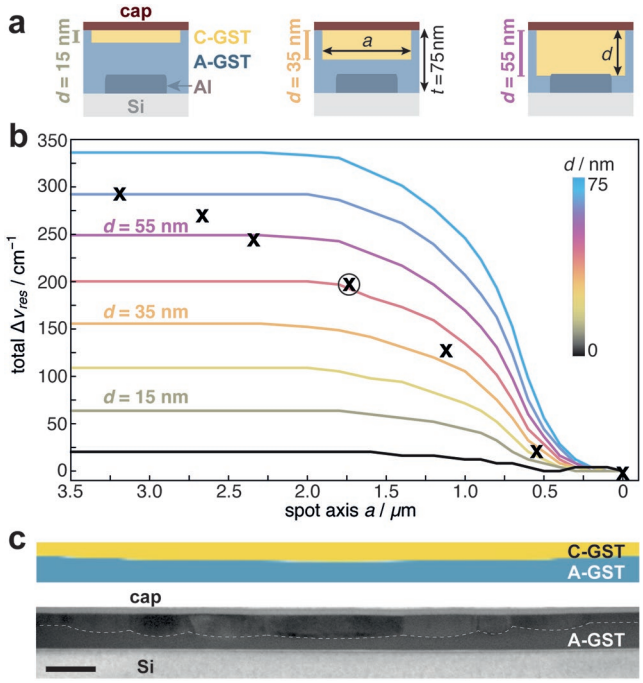

Figure 3. Importance of the crystallization depth. a) Side-view of the simulated meta-atoms for the same spot size a but different crystallization depths $d \leq t$. b) Simulated resonance shift $\Delta\nu_{res}(a,d)$ as a function of the C-spot size a and the crystallization depth d. The experimental data are plotted as crosses (cf. Figure 2b. c) Multiphysics simulation (top) and TEM image (bottom, contrast adjusted) of a C-spot cross-section without antenna. In both, it is clearly visible that $d < t$. In the TEM image, the C-spot (data point in Figure 3b marked with circle) has a crystallization depth $d \approx 47$ nm $< t = 75$ nm at its center, which decreases outwards. More details in Supporting Information. Scale bars equal 100 nm.

crystallization depth d leads to a larger resonance shift for the same C-spot size a. The experimentally obtained resonance shifts for different spot sizes a are plotted as cross marks. These crosses do not follow any one of the simulated curves for a fixed d. Rather, the data points seem to lie on different curves of increasing crystallization depth d for increasing spot size a. This indicates that C-spots of different lateral size also have different crystallization depth, which explains the trend of the resonance shift observed in the experimental data.

To verify our assumptions regarding the crystallization depth, we performed full multiphysics simulations (cf. Supporting Information) and fabricated a cross-section along the short axis of a C-spot with $a = 1.73$ µm without an antenna for transmission electron microscopy (TEM) (Figure 3c). Both simulations and TEM analysis show that the crystallization depth differs along the lateral dimensions of the C-spot while remaining smaller than the GST-film thickness. It is largest in the spot center and decreases outwards. From the TEM image shown, the crystallization depth can be measured to $d \approx 47$ nm. This fits very well to the results in Figure 3a obtained from the simulations with a simplified C-spot geometry, where $d \approx 45$ nm ($a = 1.73$ µm). Hence, these findings validate our previous assumptions and reveal the crystallization depth as a valuable additional parameter for tuning of the meta-atoms.

In conclusion, we demonstrated that we can arbitrarily tune the resonances of individual meta-atoms up to one full-width-half-maximum by optically switching localized spots on a PCM-covered infrared MS. We achieved this by precisely changing the lateral size, crystallization depth, and position of the optically crystallized spots relative to the nanoantennas. We envision that additional flexibility can be reached through controlling the crystallization depth by different thermal layer stack designs and further variation of switching laser parameters. This provides a powerful way for a free and nonvolatile programming of MSs achieved by arbitrary amplitude and phase variations of the reflected or transmitted light on the single meta-atom level. In addition to precisely tuning the operation wavelength and functionality of the whole MS, it is now also possible to make small adjustments to each meta-atom. This could for example be used to correct aberrations in holograms or lenses due to external disturbances or fabrication errors like it is common in adaptive optics.[35] The fundamental principle presented is also applicable to a multitude of active MS designs based on PCMs and not limited to metallic MSs. Low-loss dielectric MSs based on Mie resonances,[36,37] Fabry-Pérot-type resonances,[25] or surface phonon polariton resonances[31] would benefit just as much from the now accessible fine-tuning. The discussed resonance shift is always also connected to a shift in reflection phase (here max. $\pi/6$). Access to the full phase range between 0 and 2π can become available when using two overlapping resonances (e.g., electric and magnetic dipole)[36] or and additional geometric phase[19] in a adapted MS designs. Finally, the principle can be extended toward near-infrared and visible MSs by using emerging PCMs with lower optical losses in this spectral range[38–40] combined with switching lasers of shorter wavelength (deep UV)[41] to account for the smaller MS dimensions.

Experimental Section

Sample Preparation: The nanoantennas were fabricated by electron beam lithography and thermal evaporation on top of a Si substrate (area: (1×1) cm^2, thickness: 0.5 mm) with natural oxide. For patterning, a single-layer poly(methyl methacrylate)-based photoresist (thickness: 230 nm) was used. The resist was illuminated with an electron beam of 20 kV using an aperture of 10 µm. Subsequently, the samples were rinsed with developer and isopropyl alcohol. Thereafter, the metal layers, 3 nm of Cr and 27 nm of Al, were deposited by thermal evaporation with rates of about 0.4 Å s^{-1} for Cr and 1.1 Å s^{-1} for Al as measured with a quartz crystal microbalance. Excess material was removed via lift-off in acetone and the sample was rinsed in isopropyl alcohol and dried with nitrogen. The antennas were characterized using scanning electron microscopy, yielding the following antenna geometry: length $l = 642 \pm 10$ nm, width $w = 157 \pm 10$ nm, and period $p = 1259 \pm 10$ nm (cf. Supporting Information). The periodicity with $p \approx 2l$ was chosen to realize a relatively narrow resonance peak.[21] Following the nanoantenna fabrication, $t = 75$ nm of A-GST-326 and $z = 10$ nm of $(ZnS)_{80}$–$(SiO_2)_{20}$ capping layer were sputter-deposited on the substrate. A LS 320 von Ardenne systems (background pressure 2×10^{-6} mbar, 20 s.c.c.m. Ar flow, deposition rates 1.8 Å s^{-1}) was operated in constant power mode (20 W) using stoichiometric targets of 99.99% purity.

Phase-Change Materials: Germanium antimony telluride compounds $((GeTe)_x$–$(Sb_2Te_3)_{1-x}$, short: GST) are a subclass of PCMs.[42] They undergo a structural transition to the crystalline phase upon heating. A reamorphization was achieved by heating the GST above its melting

temperature T_M and rapidly cooling it back to room temperature, and thus, quenching the molten state. It was shown that these structural transitions can be achieved reversibly by single laser pulses on a sub-microsecond[31,43] and even down to a sub-picosecond timescale.[17,26] $Ge_3Sb_2Te_6$ (GST-326) was selected for our experiments because it features lower absorption losses and a higher dielectric contrast in the targeted MIR range compared to the commonly used $Ge_2Sb_2Te_5$ (GST-225) or other GST stoichiometries.[32] At a frequency of 2000 cm^{-1}, its complex refractive index changed from $\underline{n}_A = 3.5 + 0.008i$ to $\underline{n}_C = 6.12 + 0.095i$. For complete crystallization by annealing, the sample was inserted in an oven at 180 °C at ambient conditions for 30 min.

Optical Switching of the PCM: The phase change of the GST-326 thin film was realized by an in-house-built laser setup (cf. Supporting Information). Small spots of the GST-326 thin film were crystallized by applying single laser pulses on a sub-microsecond timescale with a central wavelength $\lambda = 660$ nm.[31] The laser beam was focused through a 10-fold objective with a numerical aperture of 0.5 on the sample surface. The sample was placed on a Thorlabs NanoMax-TS (Max311/M) stage, which was movable in *x*-, *y*-, and *z*-direction and connected to a Thorlabs closed-loop piezo controller (BPC303). A custom program allowed for the automated positioning of pulsed laser shots on the sample surface within 5 nm accuracy. The resulting C-spot profile was elliptical and defined by the long axis *a* and the short axis *b*. Variation of the spot size was experimentally realized by a variation of the laser pulse parameters. By varying only the pulse power *P* between ≈7 and ≈35 mW and keeping the pulse duration constant at $\tau = 450$ ns, we could reliably control the size of the C-spots on the MS between $a = 550$ nm and $a = 3190$ nm (cf. Supporting Information). In addition to erasing of the C-spots with reamorphization pulses, switching on much faster timescales was possible with this laser setup.

FTIR Spectroscopy: The Fourier transform infrared (FTIR) spectroscopy data were collected averaging over 2000 scans and with a 32 cm^{-1} resolution using a Bruker Vertex 70 interferometer coupled to a Bruker Hyperion microscope. All spectra were collected in reflection mode using a 36-fold Cassegrain objective with an average angle of incidence of about 25°. A variable knife-edge aperture of about (15×14) μm^2 defined the sample collection area. The incident light was polarized along the long axis of the antennas. The reflectance spectra shown in Figure 2a were normalized to the measured background collected from an adjacent area with no nanoantennas (Si/A-GST-326/cap). Furthermore, the spectra including a C-spot were corrected by a fit taking the aperture area, the depth *d* of the C-spots and the array coupling into account (cf. Supporting Information).

Transmission Electron Microscopy: The TEM images were taken in brightfield mode with a FEI Tecnai F20 microscope operating with 200 kV acceleration voltage and a magnification of 71 000×. Before microscopy, thin lamellae containing the cross-section of crystalline spots were prepared using focused ion beam (Helios 650 NanoLab DualBeam, FEI). In the images, contrast was given by the amount of transmitted electrons. In TEM brightfield mode, this amount stayed constant within the amorphous region contributed by mass-thickness contrast, while in crystalline regions it was dependent on the local crystallographic orientations due to different Bragg diffraction conditions. This allowed for a clear distinction between amorphous and crystalline regions and differentiating between multiple grains in polycrystalline media.[44] More detail can be found in the Supporting Information.

Simulation: Full-wave 3D simulations were performed using a commercial solver, CST Studio Suite. Excitation by Floquet Mode Ports was used to model the experiment setup and to calculate the reflectance spectra. Periodic boundary conditions were used in the lateral direction. An incident angle of 0° was assumed. The permittivity data of GST-326 was based on thin-film samples (cf. Supporting Information). For the dielectric function of aluminum, a Drude model with parameters taken from Ehrenreich et al.[45] was applied. The chromium adhesion layer was neglected in the calculations. The refractive index of silicon was assumed to be constant at $n_{Si} = 3.42$. For the thin alumina layer on top of the Al antennas, the refractive index was modeled after bulk sapphire.[46] Its thickness was assumed as 6 nm to match the literature.[47] The sample geometry was modeled according to the characterization of the fabricated samples. The size of the C-spots was varied in steps of 100 nm. The calculated resonance spectra in Figure 2a were normalized to C-spots without antennas. Details on multiphysics simulations can be found in Supporting Information.

Supporting Information

Supporting Information is available from the Wiley Online Library or from the author.

Acknowledgements

A.-K.U.M. and A.H. contributed equally to this work. The authors gratefully acknowledge the sputter deposition of the GST thin films by L. Y. Cheung. Furthermore, the authors thank C. Persch for helpful discussions regarding the laser setup and J. Barnett for his help in designing graphical elements of the paper. This work was supported by the German Federal Ministry of Education and Research within the funding program Photonics Research Germany (contract number 13N14151) and the DFG (German Science Foundation) within the collaborative research center SFB 917 "Nanoswitches". A.-K.U.M. acknowledges funding from the RWTH scholarship for doctoral students, the ETH Zurich Postdoctoral Fellowship Program, and the Marie Curie Actions for People COFUND Program. D.N.C. acknowledges a partial support by the DFG (German Science Foundation) through the Heisenberg Fellowship (CH 407/7-2).

Note: Andreas Heßler was added as a second corresponding author on July 16, 2019, after initial publication online.

Conflict of Interest

The authors declare no conflict of interest.

Keywords

active metamaterials, adaptive optics, phase-change materials, programmable metasurfaces, resonance tuning

Received: February 13, 2019
Revised: April 30, 2019
Published online: May 27, 2019

[1] N. Yu, F. Capasso, *Nat. Mater.* **2014**, *13*, 139.
[2] H.-S. Ee, R. Agarwal, *Nano Lett.* **2016**, *16*, 2818.
[3] J. Y. Ou, E. Plum, L. Jiang, N. I. Zheludev, *Nano Lett.* **2011**, *11*, 2142.
[4] M. C. Sherrott, P. W. C. Hon, K. T. Fountaine, J. C. Garcia, S. M. Ponti, V. W. Brar, L. A. Sweatlock, H. A. Atwater, *Nano Lett.* **2017**, *17*, 3027.
[5] A. Komar, Z. Fang, J. Bohn, J. Sautter, M. Decker, A. Miroshnichenko, T. Pertsch, I. Brener, Y. S. Kivshar, I. Staude, D. N. Neshev, *Appl. Phys. Lett.* **2017**, *110*, 071109.
[6] M. Lapine, I. V. Shadrivov, D. A. Powell, Y. S. Kivshar, *Nat. Mater.* **2012**, *11*, 30.
[7] O. Balci, N. Kakenov, E. Karademir, S. Balci, S. Cakmakyapan, E. O. Polat, H. Caglayan, E. Özbay, C. Kocabas, *Sci. Adv.* **2018**, *4*, eaao1749.
[8] K. Fan, X. Zhao, J. Zhang, K. Geng, G. R. Keiser, H. R. Seren, G. D. Metcalfe, M. Wraback, X. Zhang, R. D. Averitt, *IEEE Trans. Terahertz Sci. Technol.* **2013**, *3*, 702.

[9] X. Miao, B. Passmore, A. Gin, W. Langston, S. Vangala, W. Goodhue, E. Shaner, I. Brener, *Appl. Phys. Lett.* **2010**, *96*, 101111.
[10] M. J. Dicken, K. Aydin, I. M. Pryce, L. A. Sweatlock, E. M. Boyd, S. Walavalkar, J. Ma, H. A. Atwater, *Opt. Express* **2009**, *17*, 18330.
[11] M. A. Kats, R. Blanchard, S. Zhang, P. Genevet, C. Ko, S. Ramanathan, F. Capasso, *Phys. Rev. X* **2013**, *3*, 041004.
[12] M. Wuttig, N. Yamada, *Nat. Mater.* **2007**, *6*, 824.
[13] M. Wuttig, V. L. Deringer, X. Gonze, C. Bichara, J.-Y. Raty, *Adv. Mater.* **2018**, *30*, 1803777.
[14] M. Zhu, O. Cojocaru-Mirédin, A. M. Mio, J. Keutgen, M. Küpers, Y. Yu, J.-Y. Cho, R. Dronskowski, M. Wuttig, *Adv. Mater.* **2018**, *30*, 1706735.
[15] M. Wuttig, H. Bhaskaran, T. Taubner, *Nat. Photonics* **2017**, *11*, 465.
[16] X. Yin, M. Schäferling, A.-K. U. Michel, A. Tittl, M. Wuttig, T. Taubner, H. Giessen, *Nano Lett.* **2015**, *15*, 4255.
[17] Q. Wang, E. T. F. Rogers, B. Gholipour, C.-M. Wang, G. Yuan, J. Teng, N. I. Zheludev, *Nat. Photonics* **2016**, *10*, 60.
[18] C. R. de Galarreta, A. M. Alexeev, Y.-Y. Au, M. Lopez-Garcia, M. Klemm, M. Cryan, J. Bertolotti, C. D. Wright, *Adv. Funct. Mater.* **2018**, *28*, 1704993.
[19] X. Yin, T. Steinle, L. Huang, T. Taubner, M. Wuttig, T. Zentgraf, H. Giessen, *Light: Sci. Appl.* **2017**, *6*, e17016.
[20] T. Cao, G. Zheng, S. Wang, C. Wei, *Opt. Express* **2015**, *23*, 18029.
[21] A.-K. U. Michel, D. N. Chigrin, T. W. W. Maß, K. Schönauer, M. Salinga, M. Wuttig, T. Taubner, *Nano Lett.* **2013**, *13*, 3470.
[22] A. Tittl, A.-K. U. Michel, M. Schäferling, X. Yin, B. Gholipour, L. Cui, M. Wuttig, T. Taubner, F. Neubrech, H. Giessen, *Adv. Mater.* **2015**, *27*, 4597.
[23] M. Zhang, M. Pu, F. Zhang, Y. Guo, Q. He, X. Ma, Y. Huang, X. Li, H. Yu, X. Luo, *Adv. Sci.* **2018**, *5*, 1800835.
[24] W. Dong, Y. Qiu, X. Zhou, A. Banas, K. Banas, M. B. H. Breese, T. Cao, R. E. Simpson, *Adv. Opt. Mater.* **2018**, *6*, 1701346.
[25] P. Hosseini, C. D. Wright, H. Bhaskaran, *Nature* **2014**, *511*, 206.
[26] A.-K. U. Michel, P. Zalden, D. N. Chigrin, M. Wuttig, A. M. Lindenberg, T. Taubner, *ACS Photonics* **2014**, *1*, 833.
[27] Y. G. Chen, T. S. Kao, B. Ng, X. Li, X. G. Luo, B. Luk'yanchuk, S. A. Maier, M. H. Hong, *Opt. Express* **2013**, *21*, 13691.
[28] J. Tian, H. Luo, Y. Yang, F. Ding, Y. Qu, D. Zhao, M. Qiu, S. I. Bozhevolnyi, *Nat. Commun.* **2019**, *10*, 396.
[29] C. H. Chu, M. L. Tseng, C. D. Shiue, S. W. Chen, H.-P. Chiang, M. Mansuripur, D. P. Tsai, *Opt. Express* **2011**, *19*, 12652.
[30] C. H. Chu, C. D. Shiue, H. W. Cheng, M. L. Tseng, H.-P. Chiang, M. Mansuripur, D. P. Tsai, *Opt. Express* **2010**, *18*, 18383.
[31] P. Li, X. Yang, T. W. W. Maß, J. Hanss, M. Lewin, A.-K. U. Michel, M. Wuttig, T. Taubner, *Nat. Mater.* **2016**, *15*, 870.
[32] A.-K. U. Michel, M. Wuttig, T. Taubner, *Adv. Opt. Mater.* **2017**, *5*, 1700261.
[33] S. Kremers, *Dissertation*, RWTH Aachen University, **2009**.
[34] M. Schnell, A. García-Etxarri, A. J. Huber, K. Crozier, J. Aizpurua, R. Hillenbrand, *Nat. Photonics* **2009**, *3*, 287.
[35] R. Tyson, *Principles of Adaptive Optics*, CRC Press, Boca Raton, Florida, USA **2010**, p. 310.
[36] C. H. Chu, M. L. Tseng, J. Chen, P. C. Wu, Y.-H. Chen, H.-C. Wang, T.-Y. Chen, W. T. Hsieh, H. J. Wu, G. Sun, D. P. Tsai, *Laser Photonics Rev.* **2016**, *10*, 986.
[37] A. Karvounis, B. Gholipour, K. F. MacDonald, N. I. Zheludev, *Appl. Phys. Lett.* **2016**, *109*, 051103.
[38] Y. Zhang, J. B. Chou, J. Li, H. Li, Q. Du, A. Yadav, S. Zhou, M. Y. Shalaginov, Z. Fang, H. Zhong, C. Roberts, P. Robinson, B. Bohlin, C. Ríos, H. Lin, M. Kang, T. Gu, J. Warner, V. Liberman, K. Richardson, J. Hu, **2018**, http://arxiv.org/abs/1811.00526.
[39] L. Zhang, J. Ding, H. Zheng, S. An, H. Lin, B. Zheng, Q. Du, G. Yin, J. Michon, Y. Zhang, Z. Fang, M. Y. Shalaginov, L. Deng, T. Gu, H. Zhang, J. Hu, *Nat. Commun.* **2018**, *9*, 1481.
[40] W. Dong, H. Liu, J. K. Behera, L. Lu, R. J. H. Ng, K. V. Sreekanth, X. Zhou, J. K. W. Yang, R. E. Simpson, *Adv. Funct. Mater.* **2019**, *29*, 1806181.
[41] J. Siegel, D. Puerto, J. Solis, F. J. García de Abajo, C. N. Afonso, M. Longo, C. Wiemer, M. Fanciulli, P. Kühler, M. Mosbacher, P. Leiderer, *Appl. Phys. Lett.* **2010**, *96*, 193108.
[42] D. Lencer, M. Salinga, B. Grabowski, T. Hickel, J. Neugebauer, M. Wuttig, *Nat. Mater.* **2008**, *7*, 972.
[43] M. Salinga, E. Carria, A. Kaldenbach, M. Bornhöfft, J. Benke, J. Mayer, M. Wuttig, *Nat. Commun.* **2013**, *4*, 2371.
[44] M. Hafermann, P. Schöppe, J. Rensberg, C. Ronning, *ACS Photonics* **2018**, *5*, 5103.
[45] H. Ehrenreich, H. R. Philipp, B. Segall, *Phys. Rev.* **1963**, *132*, 1918.
[46] M. R. Querry, *Optical Constants*, Contractor Report, Missouri Univ-Kansas City **1985**.
[47] J. Evertsson, F. Bertram, F. Zhang, L. Rullik, L. R. Merte, M. Shipilin, M. Soldemo, S. Ahmadi, N. Vinogradov, F. Carlà, J. Weissenrieder, M. Göthelid, J. Pan, A. Mikkelsen, J.-O. Nilsson, E. Lundgren, *Appl. Surf. Sci.* **2015**, *349*, 826.